

On Performance Analysis of Diabetic Retinopathy Classification

Sanjayprabu Sivakumar^{1*}, Sathish Kumar Rangasamy¹, Saeid Jafari² and Karthikamani Ramamoorthy³

¹ *Department of Mathematics, Sri Ramakrishna Mission Vidyalaya College of Arts and Science, Coimbatore, India*

² *Professor of Mathematics College of Vestsjaelland South, Mathematical and Physical Science Foundation, 4200 Slagelse, Denmark.*

³ *Department of Electronics and Communication Engineering, Sri Ramakrishna Engineering College, Coimbatore, India*

Received 29th of March, 2023; accepted 19th of October 2023

Abstract

This paper describes the Classification of bulk OCT retinal fundus images of normal and diabetic retinopathy using the Intensity histogram features, Gray Level Co-Occurrence Matrix (GLCM), and the Gray Level Run Length Matrix (GLRLM) feature extraction techniques. Three features—Intensity histogram features, GLCM, and GLRLM were taken and, that features were compared fairly. A total of 301 bulk OCT retinal fundus color images were taken for two different varieties which are normal and diabetic retinopathy. For classification and feature extraction, a filtered image output based on a fourth-order PDE is used. Using OCT retinal fundus images, the most effective feature extraction method is identified.

Key Words: OCT, IHF, GLCM, GLRLM, GMM.

1 Introduction

Automatic diagnosis and the analysis of medical images both heavily rely on image processing techniques. The invention of image-processing technologies and Recent years has seen an increase in the incidence of eye diseases, which has caused many researchers to focus on automatic clinical and pathological image processing [1]. Experts must take their time analyzing the complete slide images because of their high resolution. To simplify this laborious procedure, computer-supported automatic image processing techniques are offered. In some circumstances, these methods can replace the end user in the expert's image-processing decision-making process[2]. The primary indication that can cause a patient blind is diabetic retinopathy [3]. According to a WHO analysis, 135 million individuals worldwide have diabetes mellitus, and by 2025, that number is expected to increase. Diabetes is a metabolic condition that appears when the pancreas malfunctions or when the body is unable to produce enough insulin [4]. Diabetic retinopathy, one of numerous diabetes-related complications, is the main reason why people go blind. The rear of the eye is primarily covered by the retina. Fluid leakage from injured blood vessels within the retinal tissue causes vision distortion. In other circumstances, the retina's surface may acquire unusual blood vessels, or the blood vessels may enlarge and leak liquid [5]. Patients with

Correspondence to: sanjayprabu@rmv.ac.in*

Recommended for acceptance by Angel D. Sappa

<https://doi.org/10.5565/rev/elcvia.1677>

ELCVIA ISSN:1577-5097

Published by Computer Vision Center / Universitat Autònoma de Barcelona, Barcelona, Spain

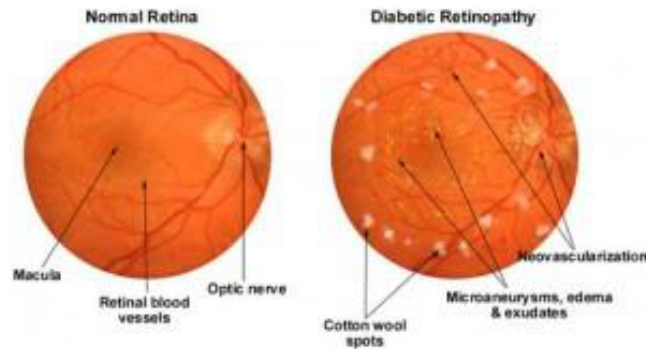


Figure 1: Normal Image vs. DR affected Image

diabetic retinopathy often don't show any symptoms until the very end. A patient having diabetic retinopathy may not show any symptoms before the problem worsens [6]. People who have this illness can lower their risk of going blind by receiving early treatment. The reflected light is used by optical coherence tomography (OCT), a noninvasive imaging method, to capture images of the retina. It can be used to identify and treat conditions like glaucoma and diabetes-related retinopathy.

Image features are employed in both the decision-making procedure and the automated classification of images. Numerous aspects of the image, including variations in texture, shape, light, and color, give information that classification systems can use. Choosing the right classification method for the appropriate features is the process's most important stage. Different feature extraction techniques can produce various categorization outcomes for the same image [7]. As a result, choosing features is a crucial stage in the classification process. Finding features with the fewest parameters that can accurately represent the image is the objective of feature extraction techniques. If the aforementioned properties are present, the image can be usefully represented with less information. By removing unnecessary parameters, a classification can be completed more quickly and successfully with less computational work [8]. Images are typically modified to remove both high-level and low-level details. Simpler image features are seen in low-level features, which require less computation. However, for complicated images, the categorization success is low. High-level features require more calculations and are more complex. Depending on the issue, several features can be used. Because of this, the literature has a wide variety of feature extraction techniques. In this work, various algorithms that can extract characteristics at greater levels have been tried on OCT retinal fundus scan images. Therefore, extracting feature data from histograms has been tried using the effective techniques described in the research study, GLCM, GLRLM, and Intensity histogram. The feature matrix for every image is extracted after each method has been applied in order to the entire dataset. These property matrices, which were created from labeled images, are sorted using GMM. The study's objective is to determine the best method for extracting features from eye images. As a result, research has been done to identify the best feature extraction methods for representing image texture as well as the GMM classification approach for comparing these methods.

Section 1 of this paper is an introduction, Section 2 describes material and methods, Section 3 provides a fourth-order PDE-based filter method, Section 4 presents various feature extraction techniques and classification, Section 5 details the experiments and their outcomes, and Section 6 summarizes the conclusions.

2 Material and Methods

2.1 Image Acquisition

The open-source Kaggle database was used in this study's classification of diabetic retinopathy. This database, which contains 301 OCT eye scans and the corresponding ground truth images, is open source and contains an analysis of each image's defects utilizing effective algorithms. Among the 301 images, 187 are normal and 114

are abnormal.

2.2 Image Preprocessing

The retinal images are preprocessed by resizing images and selecting the proper filter from the RGB image. Typically, MSE (Mean Squared Error), PSNR (Peak Signal-to-Noise Ratio), and SNR (Signal-to-Noise Ratio) are metrics used to evaluate the quality and performance of image processing algorithms, including filtering techniques. They provide quantitative measures of the distortion, noise level, and signal fidelity in processed images. Based on this PSNR, SNR, and MSE values the filter are selected. The filter should have less MSE value and high PSNR value. We choose the appropriate filter by the MSE and PSNR values. The following steps are used to prepare OCT images of the retinal for grayscale conversion from RGB images. Different resolutions of retinal images were taken for testing. All of the collected images were reduced to 256x256 pixels in order to maintain a constant resolution. Retinal images that had been scaled were in RGB color space. After that, grayscale versions of the RGB images are obtained. Additionally, this procedure is necessary because it enhances the image attributes that are important for subsequent processing while also improving the image data. For this reason, the grayscale channel is used to analyze the retinal images.

3 Fourth Order PDE based Filter

It has been researched that scale-space analysis and image enhancement (noise removal) can both benefit from the application of second-order partial differential equations (PDE). Included in these are equations for anisotropic diffusion [9].

Since the image gradient for such borders is zero, an image that is expanding towards such a levels (horizontally planar) image satisfies the boundary requirement of zero gradients. Blocky effects associated with anisotropic diffusion were very well analyzed in [10]. Assume of u , t , and c as the pixel intensity function, time, and diffusion coefficient, respectively. The following is an expression for the equation of anisotropic diffusion in (1)

$$\frac{\partial u}{\partial t} = \text{div}(c(\nabla u)\nabla u) \quad (1)$$

This equation has a relation to these energy functionals:

$$E(u) = \int_{\Omega} f(\nabla u)d\Omega \quad (2)$$

Where The diffusion coefficient and the image support Ω both have an increasing relationship with $f(\cdot) \geq 0$,

$$c(S) = \frac{f'(s)}{s} \quad (3)$$

An introduction of a fourth-order PDE category is made to efficiently improve the export among edge preservation and noise reduction. The temporal improvements in these PDEs aim to decrease a cost functionality whose absolute value is a function of the Laplacian of the image intensity function. These PDEs try to preserve edges by estimating a reported image with either a piece-wise planar image since the Laplacian of an image at the pixel is 0 if the image is planar in the region. Instead of using piecewise planar images to imitate an observed image, anisotropic diffusion (second-order PDEs) uses step images that seem more real. Thus, while eliminating the blocky impacts that are typically present in images treated by anisotropic diffusion, the suggested PDEs can be used for edge-preserving rates that are better compared to anisotropic diffusion. Despite the fact that both methods appear to be equally effective at eliminating speckles in the observed images, anisotropic diffusion frequently produces a large number of false edges, making speckles more noticeable in the images handled by the suggested PDEs.

The following functional defined over support of Ω . Initially, continuous image space would be taken into consideration.

$$E(u) = \int_{\Omega} f(|\nabla^2 u|) dx dy \quad (4)$$

Where ∇^2 denotes Laplacian operator and $f(\cdot) \geq 0$ and is an increasing function

$$f'(\cdot) \geq 0 \quad (5)$$

in order for the function to improve as $|\nabla^2 u|$ assessment of the image's clarity. Therefore, filtering the image is equivalent to minimizing the function.

$$E(u) = \int_{\Omega} F(x, y, u, D_1 u, D_2 u, \dots, D_i u, \dots) dx dy \quad (6)$$

Where

$$D_i u = \left[\frac{\partial^i u}{\partial x^i}, \frac{\partial^i u}{\partial y^i} \right]^T \quad (7)$$

The equivalent Euler equation

$$\sum D_i^T \left(\frac{\partial F}{\partial D_i u} \right) = 0 \quad (8)$$

If $D_i^T = -D_i$ stands for derivative of odd order and $D_i^T = +D_i$ for derivative of even order, For our unique situation, we have

$$F(U_{xx}, U_{yy}) = f(|\nabla^2 u|) = f(|U_{xx} + U_{yy}|) \quad (9)$$

We can easily derive that

$$\frac{\partial F}{\partial u_{xx}} = \frac{\partial F}{\partial u_{yy}} = f'(|\nabla^2 u|) \text{sign}(\nabla^2 u) \quad (10)$$

where

$$\text{sign}(s) = \begin{cases} -1, & s < 0 \\ 0, & s = 0 \\ 1, & s > 0 \end{cases} \quad (11)$$

and

$$f'(s) = \frac{\partial f}{\partial s} \quad (12)$$

Consequently, the Euler equation is

$$\nabla^2 [f'(|\nabla^2 u|) \text{sign}(\nabla^2 u)] = 0 \quad (13)$$

which is

$$\nabla^2 \left[f'(|\nabla^2 u|) \frac{\nabla^2 u}{|\nabla^2 u|} \right] = 0 \quad (14)$$

If we define

$$\frac{\nabla^2 u}{|\nabla^2 u|} \Big|_{\nabla^2 u=0} \quad (15)$$

Using (3), we may represent (14) as

$$\nabla^2 [c(|\nabla^2 u|) \nabla^2 u] = 0 \quad (16)$$

Using the gradient descent method, the Euler equation may be solved:

$$\frac{\partial u}{\partial t} = -\nabla^2 \left[f'(|\nabla^2 u|) \frac{\nabla^2 u}{|\nabla^2 u|} \right] = -\nabla^2 [c(|\nabla^2 u|) \nabla^2 u] = 0 \quad (17)$$

using the detected image as the starting point. The result is reached at time $t \rightarrow \infty$, although the development of time may have been stopped early to achieve the best possible trade-off between noise removal and edge conservation. The characteristics of a derived fourth-order diffusion equation are examined.

Assume that an image is considered to be planar if its intensity satisfies the equation for a plane. The Euler equation is satisfied by such an image since it has a 0 Laplacian (16). Additionally, we can show that a planar image is a lower bound for the cost functional $E(u)$. The functional $E(u)$ is constrained to the following values since $f(|\nabla^2 u|)$, is nonnegative:

$$E(u) \geq 0 \quad (18)$$

$f(|\nabla^2 u|)$ has a global minimum at $|\nabla^2 u| = 0$. Since it is an increasing function of $|\nabla^2 u|$. As a result, $E(u)$'s minimum occurs when

$$|\nabla^2 u| = 0 \quad \forall (x, y) \in \Omega \quad (19)$$

Evidently considering (19), a planar image is a global minimum of $E(u)$. The sole global minimum of $E(u)$ is provided by planar images. If $f(\cdot)$ is convex, or equivalently if

$$f''(s) \geq 0 \quad \text{for all } s \geq 0 \quad (20)$$

Since this circumstance exists, the cost functional $E(u)$ is convex. In order to achieve the planar image described in (17), the image is gradually smoothed down over time.

The cost functional $E(u)$ might not be convex, however, if condition (20) is not met, that is, if $f''(s) < 0$ for some or all of $s \geq 0$. As a result, further local or global minima may exist. Here, we demonstrate that such minima are piecewise planar images. Let Ω_i , be a partition of $i = 1, 2, \dots, n$. A piece-wise planar image is what we define as

$$s(x, y) = \sum_{i=1}^n s_i(x, y) \quad (21)$$

where

$$s(x, y) = \begin{cases} \text{planar image}, & (x, y) \in \Omega_i \\ 0, & \text{otherwise} \end{cases} \quad (22)$$

We demand that the composite image $s(x, y)$ in (22) be continuous from the planar images. Keep in mind that any two neighbouring $s_i(x, y)$ and $s_j(x, y)$ must be on distinct planes; if not, we can merge them into one. Let's say that Ω_i is the partition's boundary, and $\Omega_i - \partial\Omega_i$ is the interior of Ω_i . It is clear that

$$\nabla s_i(x, y) = \text{constant}, (x, y) \in (\Omega_i - \partial\Omega_i) \quad (23)$$

So we have

$$\nabla^2 s_i(x, y) = 0, (x, y) \in (\Omega_i - \partial\Omega_i) \quad (24)$$

for $i = 1, 2, \dots, n$. Therefore,

$$\nabla^2 s_i(x, y) = 0, (x, y) \in (\Omega - \partial\Omega) \quad (25)$$

where $\partial\Omega = \bigcup_{i=1}^n \partial\Omega_i$. Any two neighbouring s_i and s_j must be on distinct planes in order to be adjacent, therefore we get

$$\nabla s_i \neq \nabla s_j \quad (26)$$

Ω_i and Ω_j , any two neighbouring partitions. This suggests that the gradient near the boundary $\partial\Omega$ is not continuous. Thus, we have

$$\nabla^2 s_i(x, y) = \infty, (x, y) \in \partial\Omega \quad (27)$$

If we require that

$$f'(\infty) = 0 \quad (28)$$

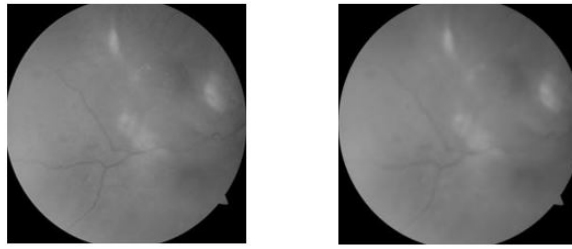


Figure 2: Original and filtered Image

We then have

$$f'(|\nabla^2 u|) \frac{\nabla^2 u}{|\nabla^2 u|} = 0 \quad \text{for all } (x, y) \in \Omega \quad (29)$$

A piecewise planar picture thus fulfils the conditions of the Euler equation. According to circumstance (5), (28) shows that $f(\cdot)$ cannot satisfy (20). Consequently, (28) suggests that

$$f''(s) < 0, \text{ for some } s \quad (30)$$

Instead, $f(\cdot)$ is not convex.

As mentioned in (28) or (30), the requirement for anisotropic diffusion to evolve an observable image into a phase image is the main cause of blocky effects in anisotropic diffusion.

Figure 2 shows grayscale conversion of original image and Fourth order PDE based filtered image. On the other hand, we believe that the proposed fourth-order PDE drives an observable image beyond a piecewise planar image, which is a good estimate to image data. As a result, the modified image will look less blocky and more real. In below Table 1 depicts the performance of the filters in OCT retinal images.

| Filters | PSNR | SNR | MSE |
|-----------------------|----------|----------|-----|
| Mean | 35.86147 | 16.86293 | 54 |
| Median | 46.34483 | 1.508682 | 59 |
| Wiener | 46.32887 | 1.514236 | 11 |
| Anisotropic Diffusion | 44.98041 | 2.065567 | 9 |
| Fourth order PDE | 45.66501 | 1.764328 | 6 |

Table 1: Filter's efficiency of the OCT images

4 Feature Extraction Techniques

The processing of OCT retinal pictures takes some time because they are relatively large. As a result, the process time is reduced while each of an image is subjected to feature extraction. Classification algorithms are used to classify these image descriptive feature matrices that were created during the feature extraction procedure. Feature extraction approaches study items and images in order to extract the much more noticeable features which are typical of the various categories of factors. Features are sent into classifiers as inputs, which categorize them into the class that features represents.

In this work, characteristics from the intensity histogram features, the Gray Level Co-Occurrence Matrix (GLCM) and Gray Level Run-Length Matrix (GLRLM) are extracted.

4.1 Intensity Histogram Features (IHF)

Six features were used for the intensity histogram analysis: mean, variance, skewness, kurtosis, energy and entropy. The discrete image can be described as $p(i, j)$, N_R is the total number of pixels in the retinal region, and the following values can be used to estimate mean, variance, skewness, kurtosis, energy and entropy [11].

| Features | Equation |
|--------------|---|
| Mean(M) | $\frac{1}{N_R} \sum_i \sum_j [p(i-k, j-l)]$ |
| Variance(V) | $\frac{1}{N_R} \sum_i \sum_j [p(i-k, j-l) - M]^2$ |
| Skewness(S) | $\frac{1}{N_R} \sum_i \sum_j [p(i-k, j-l) - M]^3$ |
| Kurtosis (K) | $\frac{1}{N_R} \sum_i \sum_j [p(i-k, j-l) - M]^4 - 3$ |
| Energy (E1) | $\frac{1}{N_R} \sum_i \sum_j [p(i-k, j-l) \cdot p(i-k, j-l)]$ |
| Entropy(E2) | $\frac{1}{N_R} \sum_i \sum_j [p(i-k, j-l) \cdot \log_2(p(i-k, j-l))]$ |

Table 2: Mathematical equations for Intensity Histogram Features

In below Table 2 shows the equations for mean, variance, skewness, kurtosis, energy and entropy respectively. Table 3 shows that the intensity histogram features values of normal and diabetic retinopathy affected images.

| Features | Normal | Abnormal |
|--------------|---------|----------|
| Mean(M) | 4.2111 | 4.7815 |
| Variance(V) | 3.0351 | 4.1464 |
| Skewness(S) | -0.8286 | -0.8967 |
| Kurtosis (K) | 2.7018 | 2.6808 |
| Energy (E1) | 0.2525 | 0.2289 |
| Entropy(E2) | 1.4933 | 1.6118 |

Table 3: Intensity Histogram Feature values for OCT Images

4.2 Gray Level Co-occurrence Matrix (GLCM)

The widely used statistical feature extraction method known as GLCM looks for the texture's nature by examining the relationships between the grey levels [12]. It is described as having a probability of 2 pixels (i, j) at which refers to the specific distance 'd' in the GLCM. It denotes the likelihood or probability that pixels (i, j) at that particular distance have similar intensities p_i and designates a square array, where the number of columns and rows matches the number of unique image levels.

Features including auto correlation, cluster prominence, cluster shade, contrast, correlation, difference entropy, difference variance, dissimilarity, information measure of correlation 1, information measure of correlation 2, energy, homogeneity, maximum probability, entropy, variance, Sum entropy, difference variance, Information measure of Correlation, sum variance, sum average, and inverse difference normalized are retrieved from the GLCM.

| Features | Equations | Features | Equations |
|---------------------|---|---------------------|---|
| Auto Correlation | $\sum_i \sum_j (i,j) p_{ij}$ | Homogeneity | $\sum_i \sum_j \frac{1}{1+(i-j)^2 p_{ij}}$ |
| Cluster Prominence | $\sum_i \sum_j (i+j-2\mu)^2 p_{ij}$ | IMC 1 | $\sum_i \sum_j \frac{HXY - HXY1}{\max(HX, HY)}$ |
| Cluster shade | $\sum_i \sum_j (i+j-2\mu)^4 p_{ij}$ | Energy | $\sum_i \sum_j p_{ij}^2$ |
| Contrast | $\sum_i \sum_j (i,j)^2 p_{ij}$ | Inverse difference | $\sum_i \sum_j \frac{p_{i,j}}{1+ i-j }$ |
| Correlation | $\sum_i \sum_j \frac{(i,j) p_{i,j} - \mu_x \mu_y}{\sigma_x \sigma_y}$ | Maximum probability | $\max_{ij} p_{i,j}$ |
| Difference entropy | $\sum_{k=0}^{N-1} p_{x-y}(k) \log p_{x-y}(k)$ | Sum average | $\sum_{k=2}^{2N} p_{x-y}(k) \log p_{x-y}(k)$ |
| Difference variance | $\sum_{k=0}^{N-1} (k - \mu_{x-y})^2 p_{x-y}(k)$ | Sum entropy | $-\sum_{k=2}^{2N} p_{x+y}(k) \log p_{x+y}(k)$ |
| Dissimilarity | $-\sum_i \sum_j i-j p_{ij}$ | Sum of squares | $\sum_i \sum_j (i-\mu)^2 p_{ij}$ |
| IMC 2 | $\sqrt{1 - \exp[-2(HXY^2 - HXY)]}$ | Sum Variance | $\sum_{k=2}^{2N} (k - \mu_{x+y})^2 p_{x+y}(k)$ |
| Entropy | $\sum_i \sum_j p_{ij} \log p_{i,j}$ | | |

Table 4: Mathematical equations for GLCM Features

Table. 4 depicts the GLCM features and its equations. The below Table. 5 shows that the GLCM feature values of normal and diabetic retinopathy images.

| GLCM Features | Normal | Abnormal | GLCM Features | Normal | Abnormal |
|---------------------|------------|-----------|-------------------------|----------|----------|
| Autocorrelation | 10.7671 | 10.399 | Homogeneity(homom) | 0.9667 | 0.9631 |
| Contrast | 0.0936 | 0.08508 | Homogeneity(homop) | 0.9655 | 0.9626 |
| Correlation(Corrm) | 0.96596 | 0.97571 | Maximum probability | 0.40829 | 0.33348 |
| Correlation (Corrp) | 0.96596 | 0.97571 | Sum of squares:Variance | 10.7182 | 10.351 |
| Cluster Prominence | 77.6250 | 125.3178 | Sum average | 6.1442 | 5.8958 |
| Cluster Shade | -6.5809844 | 3.8577057 | Sum variance | 27.0302 | 23.3577 |
| Dissimilarity | 0.07298 | 0.07650 | Sum entropy | 1.49453 | 1.8418 |
| Energy | 0.28267 | 0.20261 | Difference variance | 0.09365 | 0.08508 |
| Entropy | 1.54652 | 1.90939 | Difference entropy | 0.26406 | 0.27566 |
| INV | 0.992115 | 0.99159 | IMC1 | -0.79276 | -0.8167 |
| INN | 0.998598 | 0.99870 | IMC2 | 0.93232 | 0.96356 |

Table 5: GLCM Feature values for OCT Images

4.3 Gray Level Run-Length Matrix (GLRLM)

A common technique for obtaining statistical data obtained from diagnostic images is the GLRLM, whose entries comprise parameters defining the distributions and connections of pixel intensities [13]. Where run length refers to the total number of consecutive pixels in a certain direction that has the same level of grey as the run being evaluated [14].

The OCT retinal images can be used to derive higher-order statistical information using the run length technique. The run length of a GLRLM is determined by the level of contiguous pixels in a given direction. Counting the instances of the succeeding run within the image will allow you to approximate it. The count of travels only with the gray value i and lengths j which occur in the image along the angle θ is represented by the (i, j) th element of the gray value run length matrix $P(i, j)$ [15].

LGRE, HGRE, GLN, LRE, RLN, RP, and SRE are seven different features that were derived from the GLRLM matrix.

| Features | Equations |
|----------|---|
| SRE | $\sum_{i=1}^{N_g} \sum_{j=1}^{N_r} \frac{P(i,j)}{j^2} / \sum_{i=1}^{N_g} \sum_{j=1}^{N_r} P(i,j)$ |
| LRE | $\sum_{i=1}^{N_g} \sum_{j=1}^{N_r} j^2 P(i,j) / \sum_{i=1}^{N_g} \sum_{j=1}^{N_r} P(i,j)$ |
| GLN | $\sum_{i=1}^{N_g} (\sum_{j=1}^{N_r} P(i,j))^2 / \sum_{i=1}^{N_g} \sum_{j=1}^{N_r} P(i,j)$ |
| RP | $\sum_{i=1}^{N_g} \sum_{j=1}^{N_r} P(i,j) / N$ |
| RLN | $\sum_{i=1}^{N_r} (\sum_{j=1}^{N_g} P(i,j))^2 / \sum_{i=1}^{N_g} \sum_{j=1}^{N_r} P(i,j)$ |
| LGRE | $\sum_{i=1}^{N_g} \sum_{j=1}^{N_r} \frac{P(i,j)}{i^2} / \sum_{i=1}^{N_g} \sum_{j=1}^{N_r} P(i,j)$ |
| HGRE | $\sum_{i=1}^{N_g} \sum_{j=1}^{N_r} i^2 P(i,j) / \sum_{i=1}^{N_g} \sum_{j=1}^{N_r} P(i,j)$ |

Table 6: Mathematical Equations for GLRLM

Table. 6 depicts the GLRLM features and its equations. The below Table 7 shows that the GLRLM feature values of normal and diabetic retinopathy images.

| Features | Normal | Abnormal |
|-------------------------------------|---------|----------|
| Short Run Emphasis (SRE) | 0.3058 | 0.2925 |
| Long Run Emphasis(LRE) | 407.939 | 357.5685 |
| Gray Level Non-Uniformity (GLN) | 2617.19 | 2360.004 |
| Run Percentage (RP) | 0.3403 | 0.3482 |
| Run Length Non-Uniformity (RLN) | 2149.19 | 2048.383 |
| Low Gray Level Run Emphasis (LGRE) | 0.1059 | 0.1003 |
| High Gray Level Run Emphasis (HGRE) | 67.5764 | 88.9996 |

Table 7: GLRLM Feature values for OCT images

5 Classification

The Gaussian Mixture Model is one of the machine learning techniques (GMM). They are used to group data according to the probability distribution into two categories [15]. Applications for Gaussian mixture models are numerous. In a Gaussian Mixture Model, it is claimed that all produced data samples come from a collection of constrained Gaussian distributions. As a result, GMM simulates the distribution of a given dataset using a variety of Gaussian densities.

To provide GMM classification, we need a number of image classes λ . Let λ_k , where $k = 1, \dots, N$, represent each of the N potential image classes. Applying N classifier functions $g_k(X)$, calculating the similarities between the input X and each class of image λ_k and selecting the class of image λ_k^* are the steps in the creation of a classifier that divides a generated feature vector sequence X into N classes of images.

$$k^* = \arg \max_{1 \leq k \leq N} g_k(X) \quad (31)$$

The probability serves as the coefficient of determination in the least error rate classification:

$$g_k(X) = p(\lambda_k|X) \quad (32)$$

6 Experiments and Results

Sensitivity, Specificity, Accuracy, Error Rate, F1 Score, and MSE are taken into account when analyzing the performance of the classifier for the classification of OCT retinal images. This led to 90% of the data being

used for training and 10% being used for testing. The mathematical equations for the Performance Index's (PI) four components are listed below [16].

| | | Actual Values | |
|------------------|-------------|---------------|-------------|
| | | Positive(1) | Negative(0) |
| Predicted Values | Positive(1) | 99 | 15 |
| | Negative(0) | 35 | 152 |

Table 8: Confusion matrix for GMM classifier with IHF

| | | Actual Values | |
|------------------|-------------|---------------|-------------|
| | | Positive(1) | Negative(0) |
| Predicted Values | Positive(1) | 103 | 11 |
| | Negative(0) | 27 | 160 |

Table 9: Confusion matrix for GMM classifier with GLCM features

| | | Actual Values | |
|------------------|-------------|---------------|-------------|
| | | Positive(1) | Negative(0) |
| Predicted Values | Positive(1) | 108 | 6 |
| | Negative(0) | 19 | 168 |

Table 10: Confusion matrix for GMM classifier with GLRLM features

Using data from Table. 8, 9, and 10, the standard parameters like sensitivity, specificity, accuracy are calculated for all the feature extraction techniques. These measures are in the Table 10. The following formulas are used to find the standard parameters:

$$Sensitivity = \frac{TP}{TP + FN} * 100 \quad (33)$$

$$Specificity = \frac{TN}{TN + FP} * 100 \quad (34)$$

$$Accuracy = \frac{TP + TN}{TP + TN + FP + FN} * 100 \quad (35)$$

Below is the syntax for MSE-based classification model training:

$$MSE = \frac{1}{N} \sum_{i=1}^N (P_i - Q_i)^2 \quad (36)$$

where P_i defines the observed value for a given period, Q_i indicates the desired value for representative i , and N indicates the size of the sample per patient.

$$Error\ rate = \frac{FN + FP}{TP + TN + FN + FP} * 100 \quad (37)$$

$$Precision = \frac{TP}{TP + FP} * 100 \quad (38)$$

$$F1\ Score = \frac{2 * TP}{(2 * TP) + FN + FP} * 100 \quad (39)$$

$$Jacard\ Metric = \frac{TP}{(TP + FN + FP)} * 100 \quad (40)$$

$$Balanced\ Classifier\ Rate = \frac{Sensitivity + Specificity}{2} \quad (41)$$

$$MCC = \frac{(TP * TN) - (FP * FN)}{\sqrt{(TP + FP) * (TP + FN) * (TN + FP) * (TN + FN)}} \quad (42)$$

| Parameters | IHF | GLCM | GLRLM |
|--------------------------|----------|----------|-----------------|
| Sensitivity | 73.8806 | 79.23077 | 85.03937 |
| Specificity | 91.01796 | 93.56725 | 96.55172 |
| Accuracy | 83.3887 | 87.37542 | 91.69435 |
| MSE | 2.58E-05 | 3.17E-05 | 2.68E-05 |
| Errorrate | 16.6113 | 12.62458 | 8.305648 |
| Precision | 86.84211 | 90.35088 | 94.73684 |
| F1 Score | 79.83871 | 84.42623 | 89.62656 |
| Jacard Metric | 66.44295 | 73.04965 | 81.20301 |
| Balanced Classifier Rate | 82.44928 | 86.39901 | 90.79555 |
| MCC | 0.664925 | 0.743389 | 0.830703 |

Table 11: Classifier's Performance of the extracted feature

A calculation of the performance level of several feature extraction methods with GMM classifiers from OCT retinal images is shown in Table 11. As per the above Table 11, GLRLM feature extraction technique achieved an accuracy of 91.69435% while the intensity histogram approach achieved a lesser accuracy of 83.4% for the classification of diabetic retinopathy, while the GLRLM with Gaussian Mixture Model(GMM) classifier achieved the greatest accuracy of 91.7%.

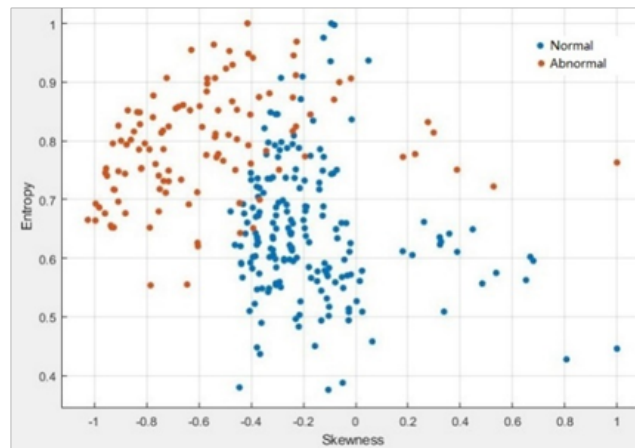


Figure 3: Scatter plot of Intensity Histogram Features

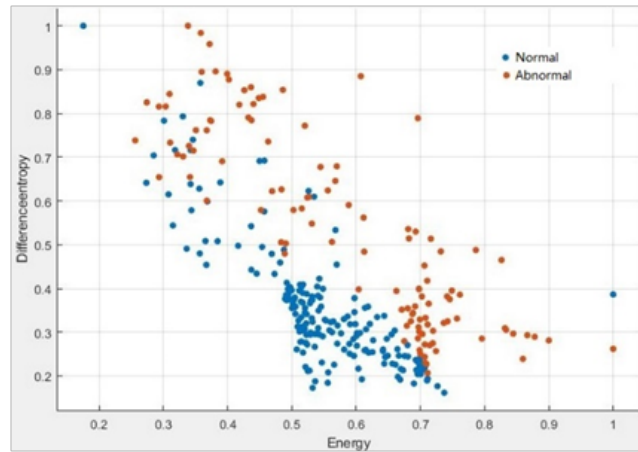


Figure 4: Scatter Plot of GLCM Features

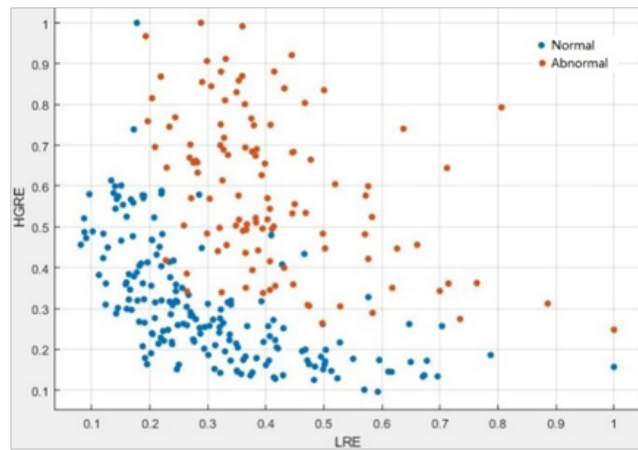


Figure 5: Scatter Plot of GLRLM Features

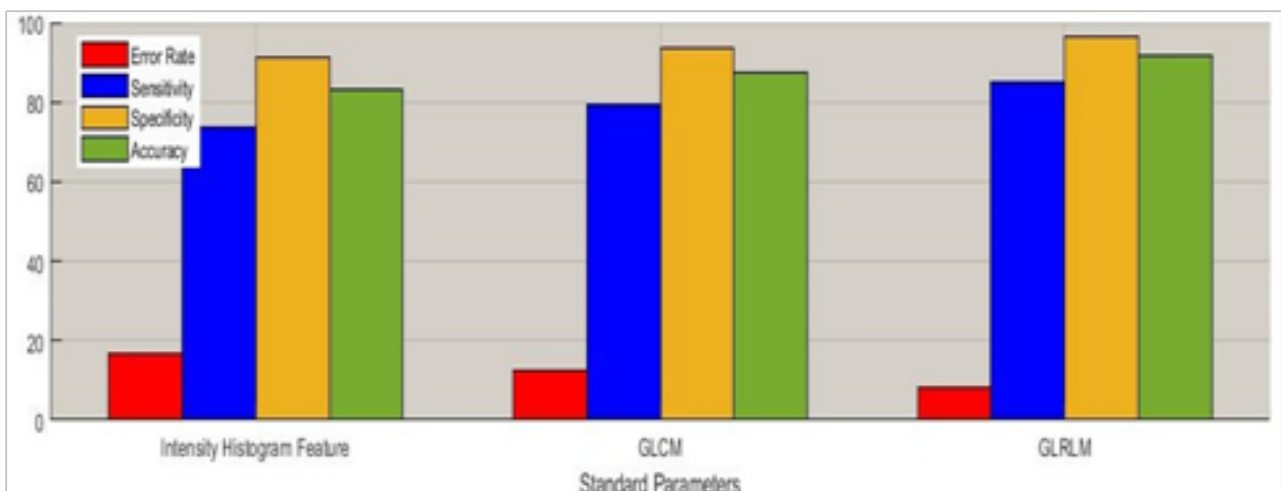


Figure 6: Graphical representation of Standard Parameters of Feature Extraction Techniques

The above figure 3, 4, and 5 show normal and abnormal case scatter plot for Intensity Histogram Features, GLCM, and GLRLM respectively. Figure 6 depicts standard parameters like error rate, sensitivity, specificity, accuracy.

and accuracy of various feature extraction techniques.

7 Conclusion

Using MATLAB software, the effectiveness of the Intensity Histogram Features, GLCM, and GLRLM feature extraction algorithms are evaluated. A fourth order PDE based filter removes image noise. This filtering is used in accordance with the MSE, PSNR, and SNR values. The average values are obtained using the GLRLM feature extraction method, and the differences between normal and abnormal images are then shown by normalizing and plotting the results. The anomaly in the retinal image is discovered using a total of three feature extraction methods. Gaussian Mixture Model (GMM) classifier with GLRLM feature extraction technique gives an average accuracy of 91.69435 percent compared to the other two feature extraction techniques to OCT scans. This approach can therefore be used to quickly identify diabetic retinopathy in a variety of datasets.

References

- [1] Sertel, O., Lozanski, G., Shana'ah, A., Gurcan, M. N., "Computer-aided detection of centroblasts for follicular lymphoma grading using adaptive likelihood-based cell segmentation", *IEEE Transactions on Biomedical Engineering*, 57(10),(2010) 2613-2616. <https://doi.org/10.1109/TBME.2010.2055058>
- [2] Mikhaylov, V. V., Bakhshiev, A. V., "The System for Histopathology Images Analysis of Spinal Cord Slices". *Procedia Computer Science*, 103 (2017), 239-243. <https://doi.org/10.1016/j.procs.2017.01.092>
- [3] I. Kocur and S. Resnikoff, "Visual impairment and blindness in Europe and their prevention", *Br. J. Ophthalmol.*, vol. 86, pp . 716722,2002.
- [4] Darshit Doshi, Aniket Shenoy, Deep Sidhpura and Dr. Prachi Gharpure, "Diabetic Retinopathy Detection using Deep Convolutional Neural Networks", *International Conference on Computing, Analytics and Security Trends*, IEEE Dec (2016), pp 261-266.
- [5] Anupama. P, Dr Suvarna Nandyal, "Blood Vessel Segmentation using Hessian Matrix for Diabetic Retinopathy Detection", *Second International Conference on Electrical, Computer and Communication Technologies (ICECCT)IEEE* (2017).
- [6] Z. A. Omar, M. Hanafi, S. Mashohor, N. F. M. Mahfudz, and M. Muna'im, "Automatic diabetic retinopathy detection and classification system", *7th IEEE International Conference on System Engineering and Technology*, (2017), pp 162-166. <https://doi.org/10.5573/JSTS.2017.17.1.162>
- [7] Nabizadeh, N., Kubat, M. (2015). Brain tumors detection and segmentation in MR images: Gabor wavelet vs. statistical features", *Computers and Electrical Engineering*, 45 (2015), 286-301. <https://doi.org/10.1016/j.compeleceng.2015.02.007>
- [8] Nagarajan, G., Minu, R. I., Muthukumar, B., Vedanarayanan, V., Sundarsingh, S. D., "Hybrid Genetic Algorithm for Medical Image Feature Extraction and Selection", *Procedia Computer Science*,85 (2016), 455-462. <https://doi.org/10.1016/j.procs.2016.05.192>
- [9] P. Perona and J. Malik, "Scale-space and edge detection using anisotropic diffusion", *IEEE Trans. Pattern Anal. Machine Intell.*, vol.12 (1990), pp. 629–639. <https://doi.org/10.1109/34.56205>
- [10] Y.-L.You,W.Xu, A. Tannenbaum, and M. Kaveh, "Behavioral analysis of anisotropic diffusion in image processing", *IEEE Trans. Image Processing*, vol. 5 (1996), pp. 1539–1553, 1996. <https://doi.org/10.1109/83.541424>

- [11] J. Ravell, M. Mirmehdi, and D. McNally, "Applied Review of Ultrasound Image Feature Extraction Methods", *Proc. of 6th Medical Image Understanding and Analysis Conference*, (2002) pp.173 – 176.
- [12] R.M. Haralick, K. Shanmugam, I. Dinstein, "Textural features of image classification", *IEEETrans. Syst. Man Cybern.* (1973) SMC-3(6).
- [13] Chu, A., Sehgal, C. and Greenleaf, J., "Use of gray value distribution of run lengths for texture analysis", *Pattern Recognition Letters* 11, (1990), 415–419, [https://doi.org/10.1016/0167-8655\(90\)90112-F](https://doi.org/10.1016/0167-8655(90)90112-F)
- [14] S. Öztürk, B. Akdemir, "Application of feature extraction and classification methods for histopathological image using GLCM, LBP, LBGLCM, GLRLM and SFTA", *Proc. Comput.Sci.* 132 (2018), 40–46. <https://doi.org/10.1016/j.procs.2018.05.057>
- [15] Manavalan R and Thangavel K, "Comparitive Analysis of Feature Extraction methods for the Classification of Prostate Cancer from TRUS Medical Images", *International Journal of Computer Science Issues*, Vol.9, No. 1, (2012).
- [16] Litjens, G., Kooi, T., Bejnordi, B.E., Setio, A.A.A., Ciompi, F., Ghafoorian, M., Van Der Laak, J.A., Van Ginneken, B., Sánchez, C.I. "A survey on deep learning in medical image analysis", *Med. Image Anal.* 42 (2017), 60–88.